Experiments in Fluids 37 (2004) 899–909
DOI 10.1007/s00348-004-0882-3

Unsteady air–water flow measurements in sudden open channel flows

Hubert Chanson

Abstract Measurements of air–water flow properties are reasonably simple in steady flows, but not so in unsteady flows. Some studies investigated periodic flows in which instantaneous data were averaged over several cycles. During the present work, new unsteady air–water flow measurements were performed in sudden open channel flow surges. Unsteady air–water flow measurements were performed in the wave front with an array of resistivity probes. The results demonstrated quantitatively strong aeration of the leading edge in terms of void fractions, bubble count rates and specific interface areas. Experimental results highlighted that this strongly aerated region was relatively short: i.e. typically 0.3 to 0.5 m long. Measurements of air and water chord sizes highlighted a wide range of bubble and droplet sizes. Time-variations of air–water flow structure were observed.

List of symbols

a	Air–water specific area (1/m) defined as the air–water interface area per unit volume of air and water
a_{mean}	Depth averaged specific interface area defined in terms of Y_{90}:
-	$a_{mean} = \frac{1}{Y_{90}} \times \int_{y=0}^{Y_{90}} a\,dy$
C	Void fraction, or air concentration, defined as the volume of air per unit volume of air and water
C_{mean}	Depth averaged air content defined in terms of Y_{90}:
-	$C_{mean} = \frac{1}{Y_{90}} \times \int_{y=0}^{Y_{90}} C\,dy$
C_s	Wave front celerity (m/s)
ch	Chord size (m)
D_o	Dimensionless constant
d_o	Equivalent dam break reservoir depth (m):
-	$d_o = \frac{9}{4} \times \sqrt[3]{\frac{Q^2}{g \times W^2}}$
d_n	Water depth (m) at the nozzle: d_n = 0.03 m in the present study
F	Bubble count rate (Hz) defined as the number of bubbles impacting the probe sensor per second
g	Gravity constant (m/s^2); g = 9.80 m/s^2 in Brisbane (Australia)
h	Step height (m)
I	Integer
K''	Dimensionless integration constant
l	Step length (m)
N_{ab}	Number of air bubbles
Q	Total volume discharge (m^3/s) of water
$Q(t = 0+)$	Initial flow rate (m^3/s)
S_o	Bed slope: $S_o = \sin\theta$
t	Time (s)
t_{ch}	Air/water chord time (s)
t_s	Time (s) of passage of the wave front at the location x'
V_o	Flow velocity (m/s) defined as: $V_o = Q/(W \times d_o)$
W	Channel width (m)
x	Horizontal longitudinal Cartesian co-ordinate (m); x = 0 at the channel intake
x'	Horizontal distance (m) measured from the vertical step height
Y_{90}	Characteristic distance (m) where C = 0.9
y	Distance (m) normal to the invert or
y	Vertical distance positive upwards

Greek symbols

ΔT	Integration time (s) corresponding to the control volume streamwise length ΔX:
-	$\Delta T = \Delta X / C_s$
ΔX	Control volume streamwise length (m): $\Delta X = I \times \Delta x$ where I is an integer equal or larger than unity
Δx	Smallest control volume streamwise length (m): Δx = 70 mm in the present study
θ	Invert slope with the horizontal
τ	Integration time (s) corresponding to the smallest control volume streamwise length Δx:
-	$\tau = \Delta x / C_s$;
ø	diameter (m)

1 Introduction

Analytical and numerical studies of air–water flows are particularly complex because of the large number of

Received: 29 May 2003 / Accepted: 7 September 2004
Published online: 30 October 2004
© Springer-Verlag 2004

H. Chanson
Department of Civil Engineering, The University of Queensland,
QLD 4072 Brisbane, Australia
E-mail: h.chanson@uq.edu.au
Fax: +61-7-33654599

The writer thanks his students C.H. Lim, C.G. Sim, C.C. Tan and Y.W. Tan for their help and assistance. He acknowledges the assistance of Dr L. Toombes (Australia).

relevant equations. Advances in measurement techniques brought new measuring systems enabling successful experiments in steady flows. Accurate measurement systems for void fraction, bubble count rates and velocity include intrusive phase-detection probes (electrical, optical), hot-film probes, fibre phase and LDA/PDA systems. Authoritative reviews include Jones and Delhaye (1976), Cartellier and Achard (1991), Bachalo (1994) and Chanson (1997, 2002). The processing of these measurement techniques is reasonably simple in steady flows, but not so in unsteady flows. Some void fraction measurements were performed in breaking waves (e.g. Hwung et al. 1992; Walkden 1999; Hoque 2002). These studies averaged void fraction measurements over half or quarter wave periods for several wave breaking events, and the results provided very coarse information on the air–water flow structure. An important contribution was the work of Stutz and Reboud (1997, 2000) in cavitating flows. They measured instantaneous gas–liquid flow properties in periodic self-oscillating flows.

All these studies investigated periodic flows in which the data could be averaged over several cycles. During the present work, new unsteady air–water flow measurements were performed in sudden open channel flow surges. They were conducted in a large size facility equipped with a flat stepped invert (θ = 3.4°). Unsteady two-phase flow properties were measured in the wave front to comprehend the wave front dynamics, its air–water flow structure and its basic properties.

2 Experimental configuration

2.1 Experimental flume

New experiments were performed in a 24 m long 0.5 m wide flume with an average bed slope S_o 0.065 (θ = 3.4°) and a stepped invert (Table 1). The flow was fed through a smooth convergent nozzle (1.7 m long). The nozzle exit was 30 mm high and 0.5 m wide. Earlier experiments (Chanson 1995) showed that steady flows downstream of the nozzle were two-dimensional and became fully developed upstream of the first drop. The nozzle was followed by a 2.4 m long horizontal invert and by 18 steps (h = 0.0715 m, l = 1.2 m). The flow rate was delivered by a pump controlled with an adjustable frequency AC motor drive Taian T-Verter K1/N1 (pulse width modulated design) enabling an accurate discharge adjustment in a closed-circuit system. Further details and the full data set were reported by Chanson (2003). Previous steady flow experiments were conducted in the same channel (Chanson and Toombes 2002a). These steady air–water flow results provide the limiting conditions of the present study.

2.2 Instrumentation

The flow rates in steady flow conditions were measured with a Dall tube flowmetre, calibrated on site with a sharp-crested weir. The accuracy on the discharge measurement was about 2%. The surging flow celerity was studied with high-shutter-speed video-cameras: i.e. a VHS video-camera Panasonic NV-RX10A (speed: 25 fr/s, shutter: sport mode, zoom: 1–14) and a digital video-camera handycam Sony DV-CCD DCR-TRV900 (speed: 25 fr/s, shutter: 1/4–1/10,000 s, zoom: 1–48). The cameras were installed above and along the axis of the channel. Additional observations were obtained using a digital still-camera Olympus Camedia C-700 (shutter: 1/2–1/1,000 s, zoom: 1–27) (Fig. 1).

Air–water flow properties were measured with a series of single-tip conductivity probes (needle probe design). Each probe consisted of a sharpened rod (platinum wire=0.35 mm) which was insulated except for its tip and set into a metal supporting tube (stainless steel surgical needle=1.42 mm) acting as the second electrode. The probes were excited by electronics designed with a response time less than 10 μs and calibrated with a square wave generator. Further details on the probe system and electronics were reported in Chanson (1995) and Cummings (1996). The probe output signals were scanned at 10 kHz per channel for 6 s. Data acquisition was triggered manually immediately prior to the flow arrival.

Visual and video observations showed that the wave front was roughly two-dimensional. Conductivity probe measurements were taken on the centreline at several distances x' from the step vertical face. At each location x', one probe (i.e. reference probe) was set on the invert, acting as a time reference, while other probes were set at different elevations (Fig. 1). The experiment was repeated until sufficient data were obtained at each vertical profile. The displacement of the probes in the direction normal to the invert was controlled by a fine adjustment travelling mechanism. The error in the probe position was less than

Table 1. Unsteady flow experimental conditions

Experiment	θ (deg.)	h m	Run	Q (t=0+) (m^3/s)	d_o (m)	Step	C_s (m/s)	Remarks
(1)	(2)	(3)	(4)	(5)	(6)	(7)	(8)	(8)
Present study	3.4	0.0715						18 horizontal steps (l=1.2 m). W=0.5 m. Nozzle depth: d_n=0.030 m.
			TL1	0.040	0.195	16	1.97	Air–water flow measurements on Step 16.
			TL3	0.055	0.241	16	2.14	Air–water flow measurements on Step 16.
			TL5	0.075	0.297	10	2.61	Air–water measurements: Steps 10 and 16.
						16	2.43	

Notes: $Q(t=0+)$: initial flow rate; d_n: approach flow depth (nozzle depth); h: step height; l: step length; C_s: average wave front celerity along the step.

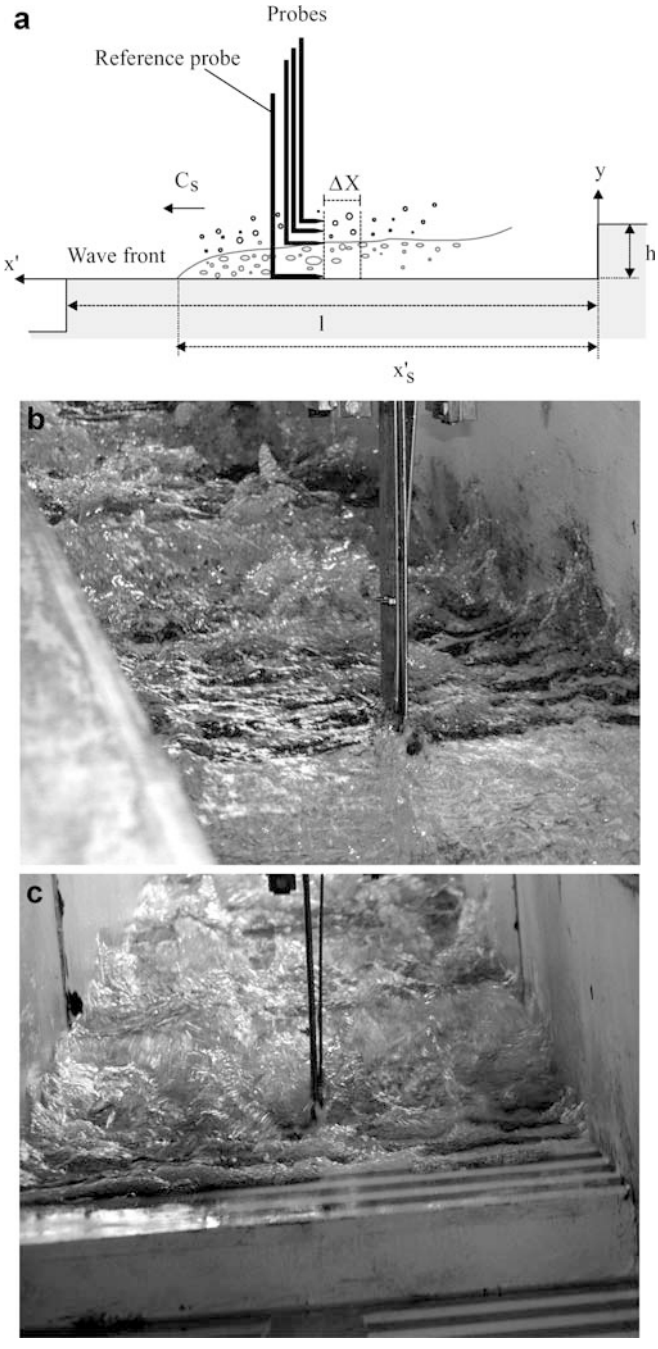

Fig. 1. Experimental channel. **a** Definition sketch. **b** Wave front flowing past the probes (flow from *top left* to *bottom right*)—Experimental run TL3—$Q(t=0+)=0.055$ m^3/s, Step 16, probe sensors: $x'=1.0$ m. **c** Wave front flowing past the probes (looking upstream)—Experimental run TL3—$Q(t=0+)=0.055$ m^3/s, Step 16

0.2 mm and 2 mm in the vertical and horizontal directions respectively.

2.3 Data processing

Video-taped movies were analysed frame-by-frame. The error on the time was less than 1/250 s, and the error on the longitudinal position of the wave front was ±1 cm. Three video recordings were taken at each location and subsequently analysed. The results in terms of wave front celerity C_s were averaged over three recordings. Average results are listed in Table 1, column 8.

In steady flows, the void fraction C is the proportion of time that the probe tip is in the air, while the bubble count rate F is the number of bubbles impacting the probe tip (e.g. Chanson 2002). In unsteady gas-liquid flows, the processing technique must be adapted. Typical conductivity probe signal outputs are presented in Fig. 2 for one flow rate at one cross-section and at three vertical elevations y above the step invert next to the leading edge of the wave front. In Fig. 2, the time origin corresponds to the first water detection by the reference probe lying on the floor.

Void fractions and bubble count rates were calculated over a short time interval τ such as $\tau = \Delta x/C_s$ where C_s is the surge front celerity measured with the video-cameras and Δx is the control volume streamwise length. A difficulty consisted in determining an optimum control volume size Δx for the moving averaging process. After preliminary tests conducted with 10 mm $\leq \Delta x \leq$ 100 mm ([1]), the basic control volume size was set at 70 mm ([2]). Such a size would contain typically 5 to 20 bubbles, and the selection was consistent with the processing technique of Stutz and Reboud (2000) who set τ to encompass at least 5 bubbles. For the data shown in Fig. 2, the short time interval τ equals: $\tau = 0.0327$ s. In the present study, the voltage signal was processed using a single threshold technique. The threshold was set at about 50% of the air–water voltage range.

Bubble count rate measurements are sensitive to the probe tip size, bubble sizes, velocity and scanning rate, particularly when the sensor size is larger than the smallest bubble sizes (e.g. Chanson and Toombes 2002b). During the present study, the bubble count rate was calculated as:

$$F = \frac{N_{ab}}{\tau} \quad (1)$$

where N_{ab} is the number of bubbles detected during the time interval τ. The measurement of air–water interface area is a function of the void fraction, velocity, bubble size and bubble count. For any bubble shape, bubble size distribution and chord length distribution, the specific air–water interface area may be estimated as:

$$a = \frac{4 \times F}{C_s} \quad (2)$$

Equation (2) is valid in bubbly flows. In high air content regions (C>0.3 to 0.5), the flow structure is more complex and the result is not exactly the true specific interface area. a becomes simply proportional to the number of air–water interfaces per unit length of air–water mixture.

[1] For Δx<10 mm, the control volume size was smaller than a fair proportion of detected bubbles. For Δx>100 mm, the averaging process did not always reflect the flow unsteadiness, especially next to the leading edge of the surging waters.
[2] Preliminary results with Δx = 50, 70 and 80 mm showed little differences between the three control volume lengths.

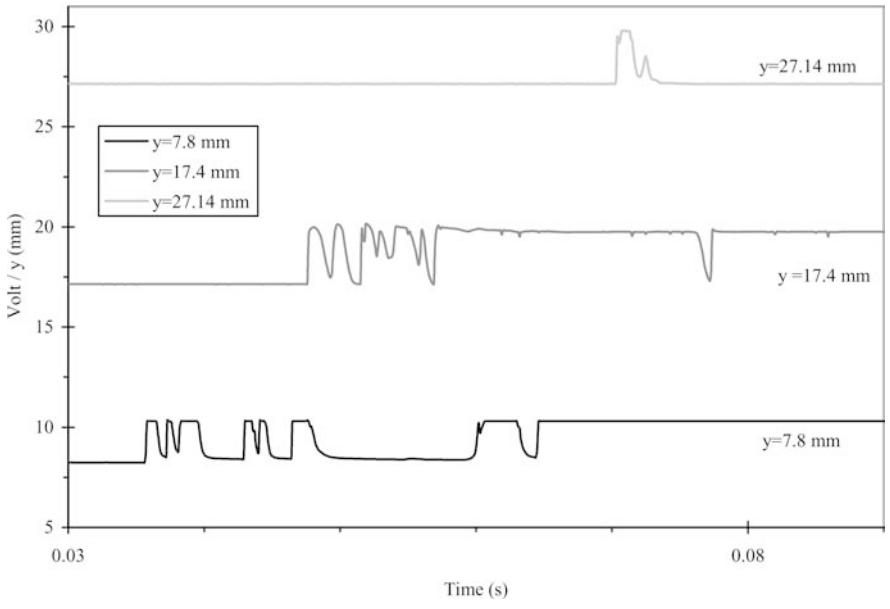

Fig. 2. Typical conductivity probe output signal—Run TL3, $Q(t=0+)=0.055$ m^3/s, Step 16, $x'=1.0$ m, $C_s=2.14$ m/s

Bubble and water chord times were measured where the bubble chord time t_{ch} is defined as the time spent by the bubble on the probe tip. The results are presented in terms of chord length *ch* defined as:

$$ch = C_s \times t_{ch} \quad (3)$$

where C_s is the wave front celerity. Equation (1) predicts accurately chord lengths near the front where the flow velocity is about the wave front speed. Note that the chord time data analysis was independent of the selection of the integration time interval τ.

2.4 Initial flow conditions

Prior to the start of each experiment, the recirculation pipe system and convergent intake were emptied. The channel was initially dry. The pump was rapidly started. The electronic controller had a 5 s ramp. The pump reached its nominal power (i.e. flow rate) at least 10 s prior to the water entering the channel. The flow rate $Q(t = 0+)$ was maintained constant until at least 10 s after the wave front reached the downstream end of the flume.

The time origin ($t = 0$) was taken as the instant when the water entered the flume. At a measurement section x', the reference time t_s was defined as the first water detection by the reference probe.

3 Experimental results

3.1 Basic flow patterns

Visual observations showed that the leading edge of the surging waters propagated basically as a nappe flow: i.e. as a succession of free-falling nappe and horizontal runoff. The wave front was highly aerated, in particular for the larger flow rates (Fig. 1b, c). Photographs highlight the chaotic nature of wave front, with strong spray, splashing and wavelets.

3.2 Void fractions

Air concentration and bubble count rate distributions were measured for three flow rates at two steps and at five locations $x'=0.2$, 0.4, 0.6, 0.8 and 1.0 m where x' is the horizontal distance from the vertical step edge (Fig. 1). Typical void fraction distributions are presented in Fig. 3 where void fractions were calculated during a short time interval ΔT such as $\Delta T = \Delta X/C_s$ where C_s is the measured surge front celerity and ΔX is the control volume streamwise length. ΔX was selected to be a multiple of Δx: i.e. $\Delta X = I \times \Delta x$ where I is an integer equal or larger than unity and Δx is the smallest control volume streamwise length (70 mm). In Fig. 3, the legend indicates the location and size of the control volume behind the leading edge of wave front: e.g. 350–735 mm means a 385 mm long control volume located between 350 mm and 735 mm behind the leading edge (Fig. 1a). In each case, the data are compared with the corresponding steady flow data. In Fig. 3, void fraction data are plotted as functions of the dimensionless distance y/d_o, where y is the distance normal to the invert and d_o is a measure of the flow rate:

$$d_o = \frac{9}{4} \times \sqrt[3]{\frac{Q(t=0+)^2}{g \times W^2}} \quad (4)$$

where $Q(t = 0+)$ is the initial flow rate and W is the channel width. (For a dam break wave down a horizontal flume, d_o would be the upstream-reservoir height.)

Figure 3 presents data at five locations x' along a single step. At $x'=0.2$ m (Fig. 3a), a free-falling nappe was observed in the early stages, although the steady flow data indicated a filled cavity. The finding is typical of all investigated flow conditions. For $x'=0.4$ to 1.0 m, the void fractions distributions exhibited a shape somehow close to self-aerated open channel flows (Fig. 3b–e). The data suggested consistently maximum flow aeration between $x'=0.4$ and 0.6 m, followed by some flow de-aeration fur-

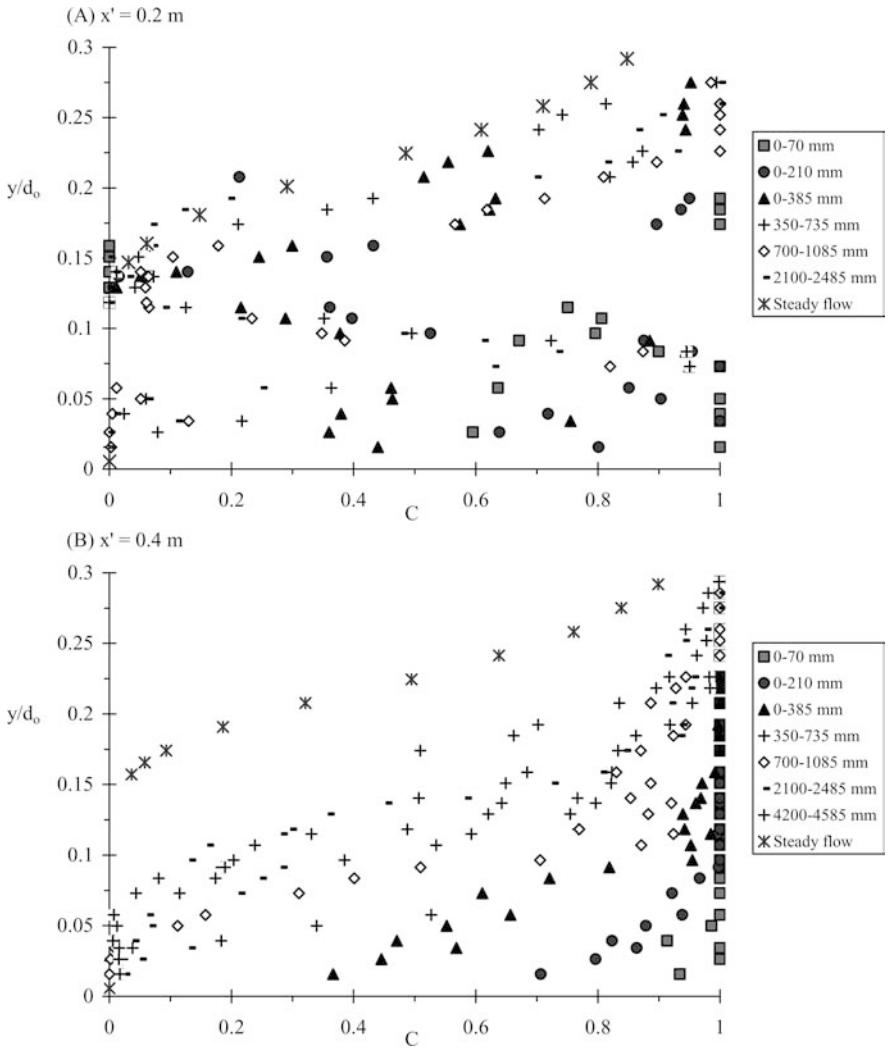

Fig. 3. Void fraction distributions behind the leading edge of wave front—Run TL5, Step 16, $Q(t=0+)=0.075$ m^3/s—Comparison with steady flow data (Chanson and Toombes 2002a)

Taba

	0–70 mm	0–210 mm	0–385 mm	350–735 mm	700–1085 mm	2100–2485 mm	4200–4585 mm
ΔX (m)=	0.070	0.210	0.385	0.385	0.385	0.385	0.385
t - t^s)$\sqrt{g/d^o}$=	0.0828	0.248	0.455	1.283	2.110	5.421	10.39

ther downstream up to x'=1.0 m. The trend is illustrated by the shape of the void fraction curves and confirmed by depth-averaged void fraction data C_{mean} (Table 2) where:

$$C_{mean} = \frac{1}{Y_{90}} \times \int_{y=0}^{Y_{90}} C \times dy \quad (5)$$

C is the void fraction and Y_{90} is the distance where C = 0.9. Mean void fraction data (Table 2) highlighted a rapid decrease in depth-averaged void fraction with increasing time (t–t_s), where t is the time and where t_s is the time of passage of wave front at a location x'.

The distributions of void fractions (Fig. 3) demonstrated consistently a strong aeration of the leading edge, especially the first 0.3–0.7 m of the wave front: i.e. $(t - t_s) \times \sqrt{g/d_o}$<1.0 to 1. The finding was consistently seen for all flow conditions and x' 0.4 m. For example, in Fig. 3e, the depth-average void fractions defined between 0 and 90% were C_{mean} = 0.86, 0.56, 0.42 and 0.21 for 0–70 mm, 0–210 mm, 0–385 mm and 700–1085 mm respectively. In steady flow, the mean air content was C_{mean} = 0.21 for the same conditions. In addition, the data highlighted a distinctive spray region (C>0.7) extending up from y = 1.5 to 2×Y_{90}.

At the front of the wave, the void fraction distributions had roughly a linear shape:

$$C = 0.9 \times \frac{y}{Y_{90}} \quad 0.1<(t - t_s) \times \sqrt{g/d_o}<1.3 \quad (6)$$

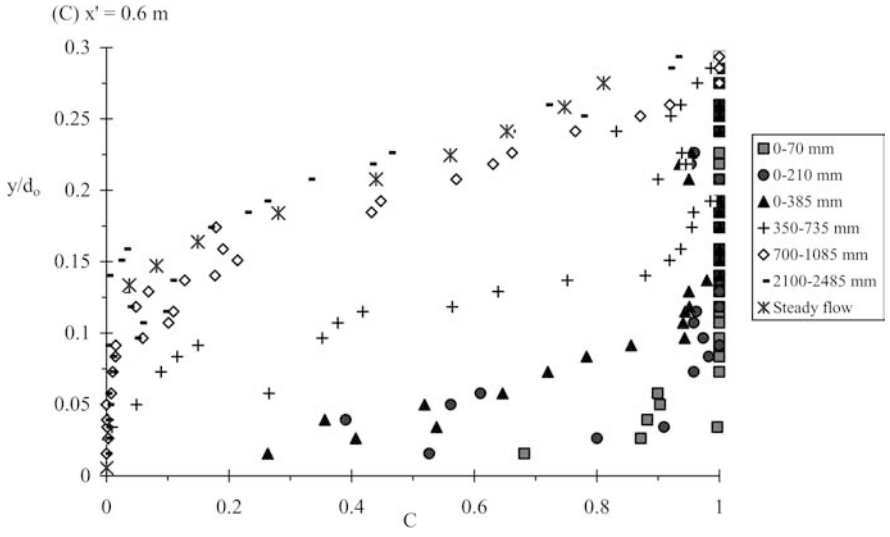

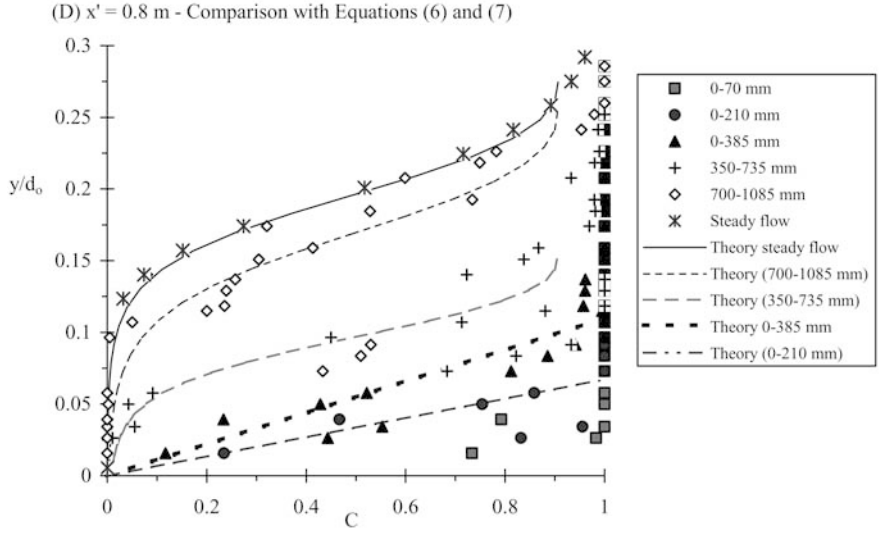

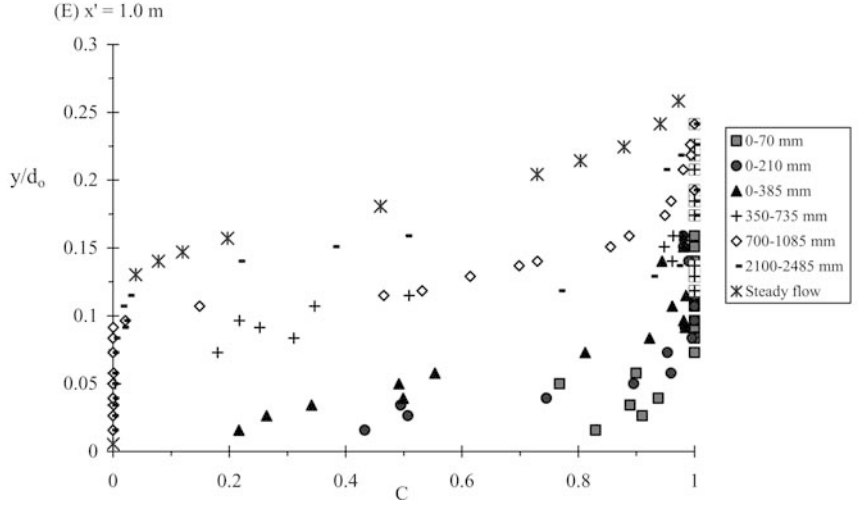

Fig. 3. (Contd.)

Equation (6) is a limiting case of an analytical solution of air bubble diffusion equation for steady transition flows down stepped chute (Chanson and Toombes 2002c). For larger times ($t-t_s$), the distribution of air concentration may be described by a diffusion model developed for steady flows:

$$C = 1 - \tanh^2\left(K'' - \frac{\frac{y}{Y_{90}}}{2 \times D_o} + \frac{\left(\frac{y}{Y_{90}} - \frac{1}{3}\right)^3}{3 \times D_o}\right) \quad (t - t_s) \times \sqrt{g/d_o} > 1.3 \tag{7}$$

Table 2. Depth averaged avoid fraction behind the leading edge of wave front—Run TL3, Step 16, $Q(t=0+)=0.075$ m^3/s—Comparison with steady flow data (Chanson and Toombes 2002a)

x (m)	C_{mean}										
	0–70 mm	0–210 mm	140–210 mm	0–385 mm	175–385 mm	350–735 mm	525–595 mm	700–1085 mm	2100–2485 mm	4200–4585 mm	Steady flow
(s)	0.0144	0.0432	0.0720	0.0792	0.1152	0.2233	0.2305	0.3673	0.9434	1.8076	+
(1)	(2)	(3)	(4)	(5)	(6)	(7)	(8)	(9)	(10)	(11)	(12)
1.0	0.86	0.56	–	0.42	0.25	0.13	–	0.21	0.21	0.27	0.21
0.8	0.77	0.43	0.39	0.46	0.26	0.35	0.20	0.31	0.24	0.22	0.24
0.6	0.76	0.63	0.47	0.53	0.36	0.25	0.29	0.24	0.22	0.24	0.29
0.4	–	0.79	0.52	0.55	0.26	0.45	0.35	0.35	0.30	0.36	0.23
0.2	Free-jet	Free-jet	Free-jet	Free-jet	Free-jet	Free-jet	Free-jet	Free-jet	Free-jet	Free-jet	0.27

Note: (–) data not available.

where K′ and D_o are functions of the mean air content only (Chanson and Toombes 2002c). Equations (6) and (7) are plotted for unsteady and steady flow conditions in Fig. 3d. The analytical models compare favourably with the data.

The results (e.g. Fig. 3) highlighted a major change in void fraction distribution shape for $(t - t_s) \times \sqrt{g/d_o} >$ 1.2 to 1.5. Possible explanations may include a non-hydrostatic pressure field in the leading front of the wave. There might be a change in air–water flow structure between the leading edge and the main flow, associated with a change in rheological fluid properties. A change in gas-liquid flow regime might take place, with a plug/slug flow regime in front and a homogenous bubbly flow region behind. This would be consistent with high-shutter speed movies of the leading edge highlighting very dynamic processes. Another explanation might be a change in shear stress distributions and boundary friction between the leading edge and the main flow behind.

3.3
Bubble count rates and air–water specific interface areas

Typical distributions of dimensionless bubble count rates and air–water specific interface areas are presented in Fig. 4. The dimensionless bubble count rate is defined as $F \times d_o/V_o$ where V_o is the characteristic velocity defined as $V_o = Q(t = 0+)/(W \times d_o)$. Specific interface area data are presented in square metres per cubic metres to emphasise the physical quantities (Fig. 4b). In Fig. 4, unsteady flow data are compared with steady flow results.

Experimental results showed consistently large bubble count rates and significant interfacial areas in the leading edge of the wave front (i.e. the first 0.2–0.3 m) for all flow conditions. Measurements showed maximum bubble count rates of up to 500 bubbles per second and specific interface areas up to 1,000 m^{-1}: that is, basically one order of magnitude greater than steady flow results. Further away from the leading edge, observed values were lower and tended to steady flow results. The finding might support the hypothesis of differences in air–water flow structure between the leading edge and the rest of the flow.

Depth-averaged air–water specific interface areas were calculated for all the data set, where the mean specific interface area was defined between 0 and Y_{90}:

$$a_{mean} = \frac{1}{Y_{90}} \times \int_{y=0}^{Y_{90}} a \times dy \quad (8)$$

Results obtained along one step are presented in Table 3, for the same data set as in Table 2. Note that different control volumes ΔX were used, while maximum depth-averaged specific interface areas were achieved for x'=0.4 to 0.6 m at $(t-t_s)$=0.043 s.

3.3.1
Discussion

Experimental results emphasised a very strong aeration of the wave front (Fig. 4, Table 3). The finding is significant because pollutants and debris are often trapped at the

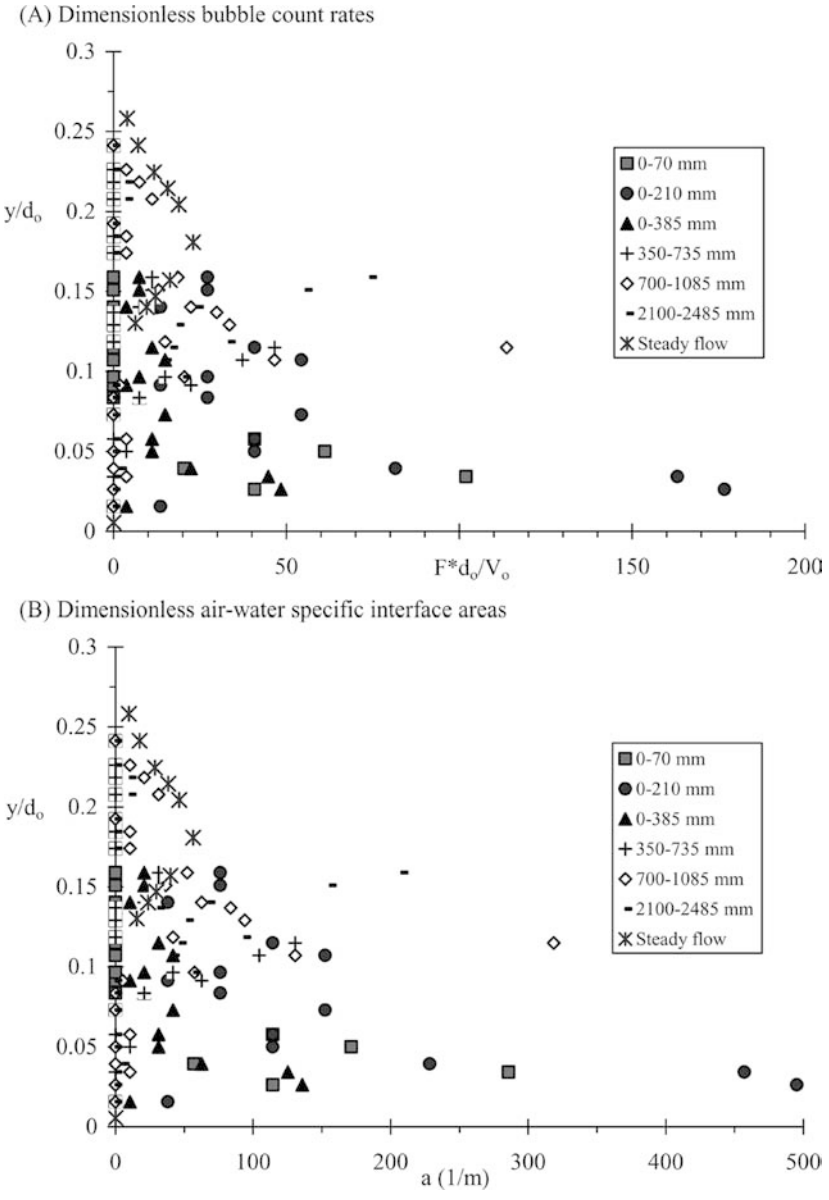

Fig. 4. Dimensionless distributions of bubble count rates and specific interface area behind the leading edge of wave front—Run TL3, Step 16, $Q(t=0+)=0.075$ m^3/s, $x'=1.0$ m—Comparison with steady flow data (Chanson and Toombes 2002a)

Tabb

	0–70 mm	0–210 mm	0–385 mm	350–735 mm	700–1085 mm	2100–2485 mm	4200–4585 mm
ΔX (m)=	0.070	0.210	0.385	0.385	0.385	0.385	0.385
t - t^s)$\sqrt{g/d^o}$=	0.0828	0.248	0.455	1.283	2.110	5.421	10.39

leading edges of surging flows (e.g. Khan et al. 2000). Strong flow aeration will contribute to oxidation of debris, pollutants and hydrocarbons collected at the leading edge of flash floods and dam break waves because the rate of mass transfer is proportional to the air–water interfacial area.

3.4 Air and water chord sizes

Chord time data analysis was conducted for all flow conditions. Typical results are shown in Fig. 5 in terms of median chord sizes. In Fig. 5, each data point represents the median air chord size at a location (x', y) during the entire study period $0 \leq (t-t_s)<6$ s. Note that the horizontal axis has a logarithmic scale and that the chord size units are millimetre.

For all investigated flow conditions, the results demonstrated consistent trends, although to a lesser extent in the free-falling nappe ($x'=0.2$ m). First the median air chord size was typically millimetric: i.e. between 1 and 10 mm (Fig. 5). Second a broad range of measured chord sizes was detected, from less than 0.5 mm to more

Table 3. Depth averaged air–water specific interface area behind the leading edge of wave front—Run TL3, Step 16, $Q(t=0+)=0.075$ m^3/s—Comparison with steady flow data (Chanson and Toombes 2002a)

x(m)	a_{mean}(1/m)									
t-t_s (s)	0–70 mm	0–210 mm	140–210 mm	0–385 mm	175–385 mm	350–735 mm	525–595 mm	700–1085 mm	2100–2485 mm	4200–4585 mm	Steady flow +
(1)	0.0144 (2)	0.0432 (3)	0.0720 (4)	0.0792 (5)	0.1152 (6)	0.2233 (7)	0.2305 (8)	0.3673 (9)	0.9434 (10)	1.8076 (11)	(12)
1.0	93.4	214.4	0.0	47.5	1.1	22.3	26.2	20.4	39.2	26.6	21.6
0.8	102.7	295.2	122.1	84.4	4.7	50.6	48.8	53.6	43.4	40.7	25.9
0.6	88.6	397.5	135.3	99.8	1.5	56.2	53.9	69.0	73.5	71.6	32.4
0.4	–	368.8	147.2	95.7	3.0	83.3	105.5	71.3	71.2	95.9	38.4
0.2	–	108.0	–	–	–	–	–	–	–	–	28.1

Note: (–) data not available.

Fig. 5. Vertical distributions of median air chord sizes for entire recordings $0 \leq (t-t_s)<6$ s (Runs TL1, TL3 and TL5)

than 25 mm. This was demonstrated by large standard deviations of chord size distributions. Third, for all flow conditions, the air chord size distributions were skewed with a preponderance of small bubble sizes relative to the mean in the bubbly flow region (i.e. $C<0.3$). The probability of bubble chord length was the largest for bubble sizes between 0 and 3 mm although the median pseudo-chord size was much larger. The trends were emphasised by positive skewness and large kurtosis (Chanson 2003).

For the largest flow rate ($Q(t = 0+)=0.075$ m^3/s), a detailed analysis of time variations in air–water flow structure was conducted at several cross-sections for $x'=0.4$ m. A typical example is shown in Fig. 6 in terms of median air/water chord sizes calculated for relatively small control volumes ($\Delta T = 0.158$ s, $\Delta X = 0.385$ m). In Fig. 6, the median chord sizes (in millimetres) are plotted as a function of the relative depth y/Y_{90}. Note that the horizontal scale differs between Fig. 6a and b. At the wave leading edge (0–385 mm), air and water chord sizes were comparable with median sizes of about 3–6 mm. This might suggest that individual bubble entrainment was associated with the ejection of water droplet of similar size. For larger times (i.e. $(t - t_s) \times \sqrt{g/d_o} > 0.5$), the order of

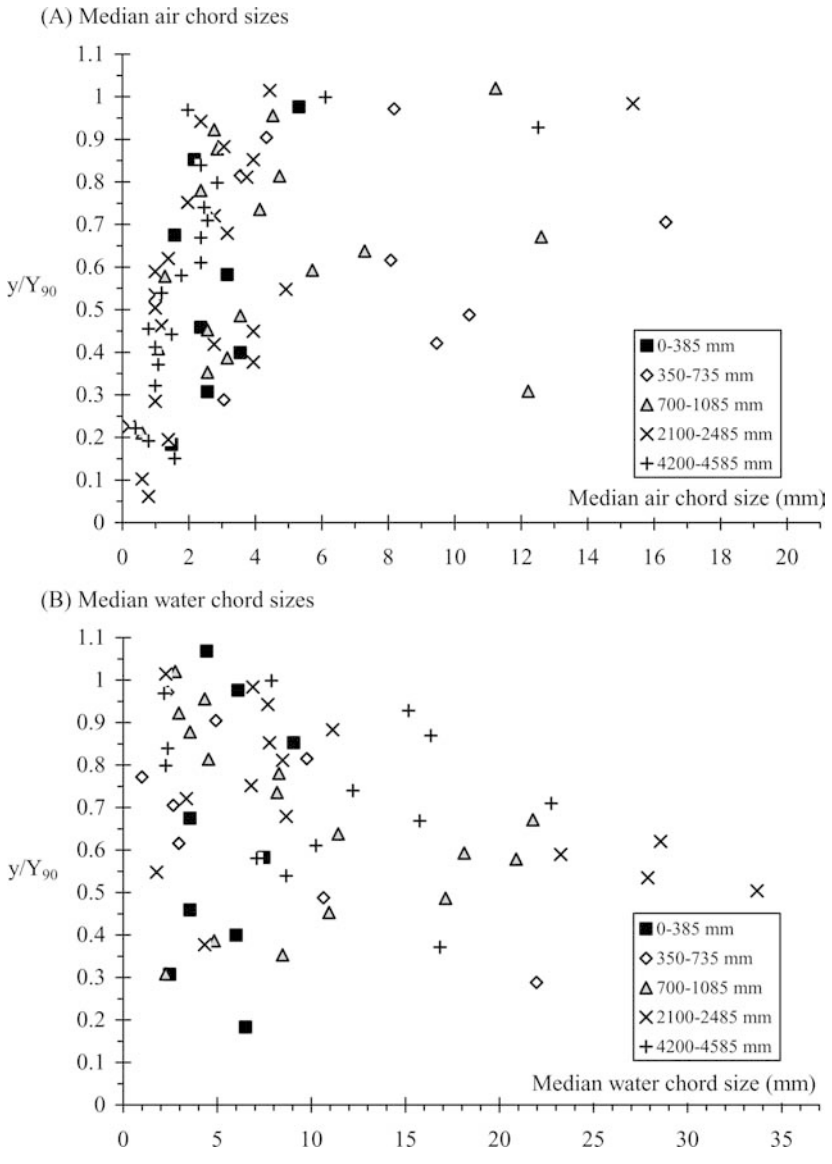

Fig. 6. Vertical distributions of median chord sizes in small streamwise control volumes (ΔX=385 mm) at several dimensionless times $(t - t_s)\sqrt{g/d_o}$—Run TL5, $Q(t$=0+)=0.075 m^3/s, Step 16, x'=0.8 m

Tabc

	0–385 mm	350–735 mm	700–1085 mm	2100–2485 mm	4200–4585 mm
ΔX (m)=	0.385	0.385	0.385	0.385	0.385
$t - t^s)\sqrt{g/d^o}$=	0.455	1.283	2.110	5.421	10.39

magnitude of median air chord sizes remained basically constant and independent of time. But water chord sizes tended to increase with time, especially for y/Y_{90}<0.7. Such a different behaviour might be related to fundamental differences between air bubbles and water droplets.

Water droplets have a momentum response time about 46,000 times larger than that of an air bubble of identical diameter (e.g. Crowe et al. 1998). As the bubble response time is significantly smaller than the characteristic time of the flow, bubble trapping in large-scale turbulent structures is a dominant mechanism in the bubbly flow region. Bubbles may remain trapped for very long times; the bubbly flow structure has some memory of its past, and it is affected by its previous structure. In the spray region, drop formation results from surface distortion, tip-streaming of ligaments and interactions between eddies and free-surface (e.g. Hoyt and Taylor 1977; Rein 1998). Once ejected, the droplet response time is nearly two orders of magnitude larger than the airflow response time. Most droplets have a short life and the spray region has little memory of its past. The spray structure may then change very rapidly in response to changes in flow con-

ditions, while the bubbly flow region is deeply affected by its earlier structure.

4 Summary and discussion

New flood wave experiments were conducted systematically down a 24 m long flat waterway with a stepped invert. Unsteady air–water flow measurements were performed in the wave front using an array of resistivity probes. A new processing technique was developed to analyse the unsteady flow data.

The results demonstrated quantitatively strong aeration of the leading edge. Bubble count rate and specific interface area data highlighted large interfacial areas in the wave front, with depth-averaged specific interface areas of up to 400 m^{-1}. Such large interfacial areas enhance air–water mass transfer at the wave front. Experimental results highlighted that the strongly aerated flow region at the leading edge was relatively short: i.e. typically 0.3 to 0.5 m long corresponding to $(t - t_s) \times \sqrt{g/d_o} < 0.5$. Behind the flow properties tended rapidly towards steady flow characteristics.

Measurements of air and water chord sizes highlighted a wide range of bubble and droplet sizes. The median air chord sizes were typically between 1 and 10 mm. Time-variations of air–water flow structure were observed. At the leading edge entrained bubbles and ejected droplets had similar sizes. Behind, however, the median water chord sizes increased with time, although the bubble sizes did not change.

References

Bachalo WD (1994) Experimental methods in multiphase flows. Int J Multiphase Flow 20:261–295

Cartellier A, Achard JL (1991) Local phase detection probes in fluid/fluid two-phase flows. Rev Sci Instrum 62(2):279–303

Chanson H (1995) Air bubble entrainment in free-surface turbulent flows. Experimental investigations report CH46/95, Dept of Civil Engineering, University of Queensland, Australia, June, ISBN 0-86776-611-5

Chanson H (1997) Air bubble entrainment in free-surface turbulent shear flows. Academic, London, ISBN 0-12-168110-6

Chanson H (2002) Air–water flow measurements with intrusive phase-detection probes: Can we improve their interpretation? J Hyd Eng ASCE 128(3):252–255

Chanson H (2003) Sudden flood release down a stepped cascade: Unsteady air–water flow measurements applications to wave run-up, flash flood and dam break wave. Report no CH51/03, Dept of Civil Engineering, The University of Queensland, Brisbane, Australia, January

Chanson H, Toombes L (2002a) Energy dissipation and air entrainment in a stepped storm waterway: An experimental study. J Irrigation Drainage Eng ASCE 128(5):305–315

Chanson H, Toombes L (2002b) Experimental study of gas-liquid interfacial properties in a stepped cascade flow. Environ Fluid Mech 2(3):241–263

Chanson H, Toombes L (2002c) Air–water flows down stepped chutes: Turbulence and flow structure observations. Int J Multiphase Flow 27(11):1737–1761

Crowe C, Sommerfield M, Tsuji Y (1998) Multiphase flows with droplets and particles. CRC Press, Boca Raton, USA

Cummings PD (1996) Aeration due to breaking waves. PhD thesis, Dept of Civil Eng, University of Queensland, Australia

Hoque A (2002) Air bubble entrainment by breaking waves and associated energy dissipation. PhD thesis, Dept of Architecture and Civil Eng, Toyohashi University of Technology, Japan

Hoyt JW, Taylor JJ (1977) Waves on water jets. J Fluid Mech 83(1):119–127

Hwung HH, Chyan JM, Chung YC (1992) Energy dissipation and air bubbles mixing inside surf zone. In: Proc 23rd Int Conf Coastal Eng, ASCE, Venice, Italy, 1(22):308–321

Jones OC, Delhaye JM (1976) Transient and statistical measurement techniques for two-phase flows: A critical review. Int J Multiphase Flow 3:89–116

Khan AA, Steffler PM, Gerard R (2000) Dam-break surges with floating debris. J Hyd Eng ASCE 126(5):375–379

Rein M (1998) Turbulent open-channel flows: Drop-generation and self-aeration. J Hyd Eng ASCE 124(1):98–102 and discussion: 125(6):668–670

Stutz B, Reboud JL (1997) Experiments in unsteady cavitation. Exp Fluids 22:191–198

Stutz B, Reboud JL (2000) Measurements within unsteady cavitation. Exp Fluids 29:545–552

Walkden MJA (1999) Model wave impulse loads on caisson breakwaters: Aeration, scale and structural response. PhD thesis, University Plymouth, UK